GS-Blur: A 3D Scene-Based Dataset for Realistic Image Deblurring

Dongwoo Lee[1] **Joonkyu Park**[1] **Kyoung Mu Lee**[1,2]
[1]Dept. of ECE&ASRI, [2]IPAI, Seoul National University, Korea
`{dongwoo.lee, jkpark0825, kyoungmu}@snu.ac.kr`

Abstract

To train a deblurring network, an appropriate dataset with paired blurry and sharp images is essential. Existing datasets collect blurry images either synthetically by aggregating consecutive sharp frames or using sophisticated camera systems to capture real blur. However, these methods offer limited diversity in blur types (blur trajectories) or require extensive human effort to reconstruct large-scale datasets, failing to fully reflect real-world blur scenarios. To address this, we propose GS-Blur, a dataset of synthesized realistic blurry images created using a novel approach. To this end, we first reconstruct 3D scenes from multi-view images using 3D Gaussian Splatting (3DGS), then render blurry images by moving the camera view along the randomly generated motion trajectories. By adopting various camera trajectories in reconstructing our GS-Blur, our dataset contains realistic and diverse types of blur, offering a large-scale dataset that generalizes well to real-world blur. Using GS-Blur with various deblurring methods, we demonstrate its ability to generalize effectively compared to previous synthetic or real blur datasets, showing significant improvements in deblurring performance. The dataset is available at: https://github.com/dongwoohhh/GS-Blur

1 Introduction

Single-image deblurring is a crucial challenge in image restoration, focusing on removing blur caused by motion between the camera and objects. To address this, pioneering approaches [23, 11, 37, 3] have proposed paired datasets, consisting of blurry images and their corresponding sharp images, designed for training deep neural networks. Specifically, their efforts to create deblurring datasets have primarily relied on two methods: *synthetic* [23, 22, 46] and *real* [47, 30, 29] data generation. However, both approaches heavily depend on heuristic human capture techniques, often leading to limitations such as incomplete coverage of large-scale datasets and inadequate representation of diverse blur types (*i.e.*, blur length and directions).

Since capturing blurry and sharp images simultaneously with a single sensor is challenging, earlier methods [35, 22, 33, 14] have resorted to synthetically generating blurry images from consecutive sharp frames. They achieve this by capturing consecutive sharp frames using high-speed cameras and then aggregating these neighboring frames to create synthetic blurry images. Although this allows for easy generation of blurry images, the resulting blur is derived from highly discrete frames, which leads to differences from real-world blur and fails to generalize well to real-world blurry images.

Later methods [47, 30, 29] have introduced specialized camera systems equipped with beam-splitters. These systems divide the light entering the camera lens into two image sensors with varying exposure times, producing sharp images from the shorter and blurry images from the longer-exposed sensor. While they generate a more realistic blur, making it better suited for real-world applications, they present several challenges. First, they require precise camera system design, complicating the use of diverse camera models. Indeed, [47] and [30] obtained their datasets from a single camera model, the

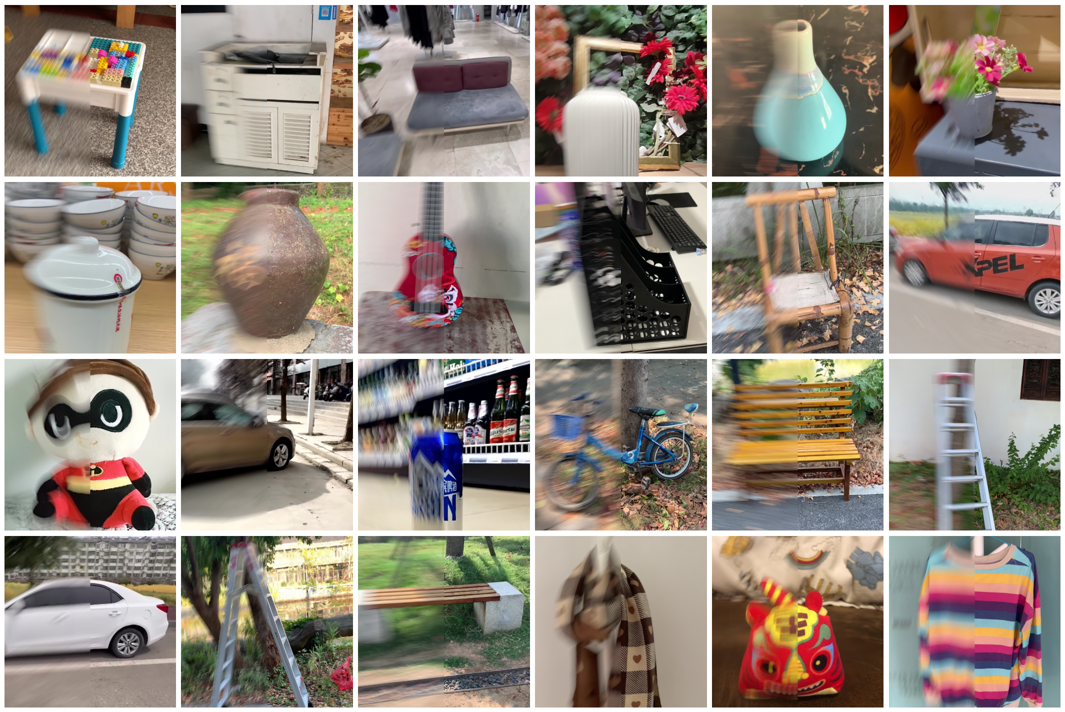

Figure 1: **Examples of the proposed GS-Blur dataset.** The left half of the frames displays synthetically generated blur, while the right half exhibits sharp pairs.

Sony A7R3 and machine vision camera, respectively. Second, despite the use of different exposure times for the two sensors, one capturing blurry images and the other sharp images, discrepancies in image signal processing (ISP) can arise, requiring additional image processing such as white balancing and color mapping. Moreover, the datasets heavily rely on human capture, which limits their scale and results in restricted blur trajectories in terms of blur length and direction.

In this paper, we explore methods to synthesize realistic blurry images to improve deblurring quality for real-world blurry images generally. To this end, we present a novel dataset, GS-Blur, which synthesizes blurry images using 3D Gaussian Splatting (3DGS) [9]. Specifically, we utilize the existing large-scale multi-view dataset, MVImgNet [43], to train 3DGS on sharp multi-view images, enabling the reconstruction of 3D scenes. Then, from these reconstructed scenes, we use two camera views to render images: one from a fixed position and one from a moving position along randomly generated motion trajectories, corresponding to sharp and blurry images, respectively. Specifically, following the method in [23, 22, 46], we aggregate multiple images from cameras along the trajectory to create blurry images, but unlike [23, 22, 46]'s use of highly discrete frames, we employ denser frames by positioning multiple cameras along the trajectories, resulting in more realistic blur. Moreover, by utilizing various degrees for the blur trajectories, our GS-Blur dataset includes diverse blur trajectories in terms of both blur length and direction. By using MVImgNet, which consists of large-scale multi-view images from diverse camera models, our GS-Blur provides diverse deblurring image pairs with significant advantages, showing generalizability, as detailed in the experiments Section 4.3. Additionally, we conduct comprehensive ablation studies to justify the reconstruction of our GS-Blur dataset in Section 4.4. The samples of GS-Blur are shown in Figure 1.

2 Related Works

Image deblurring methods. As blur commonly occurs in various situations [31, 24, 25, 28], early deblurring methods [11, 23, 26, 27, 3, 45, 15] modeled a blurry image as a convolution of a 2D blur kernel with a latent sharp image, optimizing the sharp image for a known blur kernel using Richardson-Lucy deconvolution. However, these methods struggled with real-world scenarios where

Table 1: **Comparison of existing datasets with our new GS-Blur dataset.**

Dataset	Method	Scale	Exp. time (ms)	Resolution	Need ISP
DVD [35]	Synthetic	6,708	25	1280 × 720	✗
GoPro [23]	Synthetic	3,214	25-50	1280 × 720	✗
REDS [22]	Synthetic	30,000	25-50	1280 × 720	✗
HIDE [33]	Synthetic	8,422	41.667	1280 × 720	✗
HFR-DVD [14]	Synthetic	13,500	40	960 × 540	✗
BSD [47]	Real	33,000	1-24	640 × 480	✓
RealBlur [30]	Real	4,738	500	680 × 772	✓
RSBlur [29]	Real+Synthetic	13,358	100	1920 × 1200	✓
GS-Blur	Synthetic	156,209	Various	Various	✗

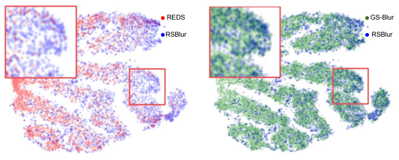

(a) Real vs Synthetic (b) Real vs **GS-Blur**

Figure 2: **Motion distribution visualization of synthetic, real, and GS-Blur datasets.**

blur kernels are unknown. Later, deep learning shifted the field to learning-based approaches, with models like DeblurGAN [11] and DeepDeblur [23] restoring sharp images without blur kernel estimation. Advanced models such as NAFNet [3] and Restormer [45] use channel attention modules, while SwinIR [15] introduce Vision Transformer [5, 18] architectures. Despite architectural advances, these methods are data-driven, requiring extensive training data that aligns well with real-world blur for effective generalization.

Deblurring datasets. Table 1 shows the overview of deblurring datasets. Earlier, several synthetic datasets [35, 23, 22, 33, 14, 46] using high-speed cameras have been proposed to train learning-based deblurring methods. DVD [35], GoPro [23], and REDS [22] create blurry images by averaging consecutive sharp frames to simulate motion blur. Similarly, HIDE [33] synthesizes blur with densely annotated foreground human bounding boxes, and HFR-DVD[14] uses a higher-speed camera (*e.g.*, SONY DSC-RX10 IV) to capture video frames, resulting in more realistic blurs. However, even with high-speed cameras, the time interval between frames is too discrete to accurately capture continuous real-world blur patterns, resulting in less effective generalization to real-world blurry images.

Other approaches [47, 30, 29] use beam splitter camera systems to capture paired images, addressing synthetic dataset limitations. These systems capture blurry images with longer exposure and sharp images with shorter exposure, accurately mimicking real-world blur. However, they face several challenges. First, they require the precise design of the camera system, which is a labor-intensive task. Moreover, due to the need for a sophisticated system, these datasets are restricted to specific camera models, showing less generalizability to blurry images captured by different cameras. Despite the implementation of the specialized camera system, utilizing different exposure times for the two image sensors, where one captures blurry images and the other sharp images, can lead to discrepancies in different light intensities reaching each sensor. This difference requires processing the images with different ISO settings, leading to disparities in tone or color between the blurry and sharp images. As a result, additional ISP processing is required to match them. Furthermore, their motion trajectories highly rely on humans, failing to capture the diverse blur patterns found in real-world scenarios.

In contrast, our GS-Blur, though synthetically derived, offers greater scale, diverse exposure times, and various resolutions compared to previous datasets, as shown in Table 1. Furthermore, the motion trajectories in GS-Blur are randomly generated in 3D space, effectively encompassing potential real-world motion trajectories. Figure 2 compares the motion trajectory distributions of synthetic [22] and real deblurring datasets [29] with our GS-Blur dataset. Here, each point in the figure represents the t-SNE [39] projection of a motion trajectory, computed using the optical flow [38] from the provided consecutive sharp frames. As shown in Figure 2a, the distribution of the synthetic dataset (●) does not overlap with the distribution of the real dataset (●), indicating that the previous synthetic dataset fails to cover the motion diversity of real-world images. On the other hand, Figure 2b shows that the distribution of GS-Blur (●) overlaps with the real distribution, demonstrating that GS-Blur covers most real blurry images' distributions and exhibits a wider range of blur diversity.

Novel view synthesis. Unlike previous synthetic datasets that simulate blur by aggregating images, our approach recovers 3D scenes and moves the view within these 3D spaces to mimic camera shakes with varying trajectories, making our work closely related to novel view synthesis. Earlier, Neural Radiance Fields (NeRF) [20] made significant strides in 3D vision tasks, particularly in photo-realistic novel view synthesis. Despite the potential of NeRF's implicit neural representation (INR) to become a widely used 3D representation, NeRF-based methods [36, 6, 1, 21] face challenges in achieving real-time novel view synthesis without compromising visual quality. To address this, 3D Gaussian Splatting (3DGS) [9] streamlines the NeRF framework through point-based 3D Gaussians and tile-based rasterization, enabling high-quality, real-time novel view synthesis at 1080p resolution.

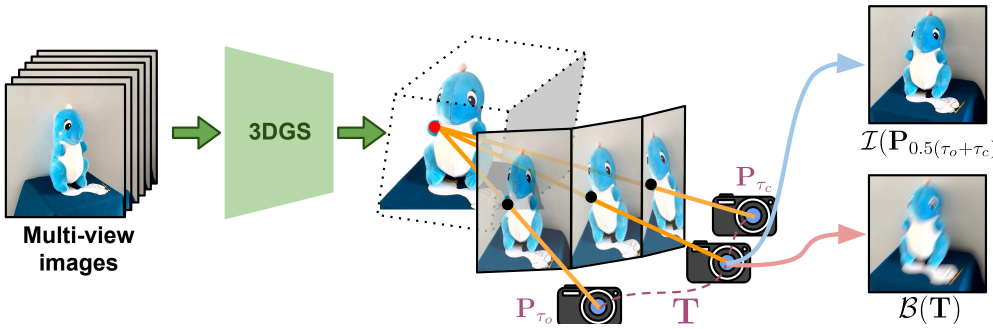

Figure 3: **The overall pipeline for generating blurry and sharp image pairs in our GS-Blur dataset.** To this end, we first train a 3D Gaussian Splatting model to reconstruct 3D scenes from multi-view images. Then, from these reconstructed 3D scenes and randomly generated motion trajectory $\mathbf{T}$, we render sharp images $\mathcal{I}(\mathbf{P}_{0.5(\tau_o+\tau_c)})$ from a fixed camera view and blurry images $\mathcal{B}(\mathbf{T})$ from a moving camera view. Specifically, we render $\mathcal{M}$ sharp images along the motion trajectory and then average these sharp frames to synthesize the blurry image.

3 GS-Blur dataset

3.1 Preliminary: 3D Gaussian Splatting

3D Gaussian Splatting (3DGS) [9] models a 3D scene from multi-view images using Gaussian primitives $\{\boldsymbol{\mu}_k, \boldsymbol{\Sigma}_k, \sigma_k, \boldsymbol{S}_k\}_{k\in\mathcal{K}}$, where each parameter represents the position $\boldsymbol{\mu}_k$, covariance $\boldsymbol{\Sigma}_k$, opacity σ_k, and spherical harmonic coefficients $\boldsymbol{S}_k$ of a sparse 3D point $k \in \mathcal{K}$, initialized from SfM [32]. When rendering an image, the Gaussian primitives are projected onto the camera's image plane, and the color of each pixel $\boldsymbol{p}$ is computed using point-based α-blending [48] as follows:

$$\hat{C}(\boldsymbol{p}) = \sum_{k\in\mathcal{K}} \alpha_k \mathbf{c}(\mathbf{v}_k; \boldsymbol{S}_k) \prod_{j=1}^{k-1}(1-\alpha_j), \tag{1}$$

$$\text{where} \quad \alpha_k = \sigma_k e^{-\frac{1}{2}(\boldsymbol{p}-\boldsymbol{\mu}_k^{\downarrow})^T \boldsymbol{\Sigma}_k^{\downarrow-1}(\boldsymbol{p}-\boldsymbol{\mu}_k^{\downarrow})}. \tag{2}$$

The color of the k-th Gaussian is computed using the spherical harmonic function $\mathbf{c}(\mathbf{v}_k; \boldsymbol{S}_k)$ for the camera's viewing direction $\mathbf{v}_k$, and the density α_k is determined from the 2D projected Gaussian weights $\boldsymbol{\mu}_k^{\downarrow}$ and $\boldsymbol{\Sigma}_k^{\downarrow-1}$ as introduced in [48]. The point-based α-blending in Equation 1 essentially follows the same image formation model as NeRF [20]. However, compared to NeRF, the explicit representation of Gaussian primitives allows for significantly faster rendering. Specifically, the cost-effective Gaussian rasterization replaces the computationally intensive multi-layer perception and ray-point sampling approach used in NeRF. As a result, 3DGS achieves high-quality real-time view synthesis and reduces training time to tens of minutes. In this work, we use the fast training and rendering speeds of 3DGS to generate realistic blurry images by densely sampling views along a moving camera trajectory.

3.2 Preliminary: MVImgNet dataset

MVImgNet [43] is a large-scale multi-view image dataset comprising 6.5 million frames from 219,199 videos, covering objects from 238 classes. These videos are captured using various common cameras (*e.g.*, smartphones), reflecting a diverse range of real-world image distributions. On this basis, we leverage this dataset to reconstruct our GS-Blur dataset. Specifically, we manually selected 26 classes suitable for constructing a deblurring dataset, with the detailed class information provided in our appendix.

3.3 Pipeline for blur synthesis of GS-Blur

Figure 3 provides an overview of the construction process for our GS-Blur dataset. To collect GS-Blur, we first train 3DGS using a set of $\mathcal{N}$ posed sharp images $\{\mathcal{I}(\mathbf{P}_i)\}_{i\in\mathcal{N}}$ with their corresponding

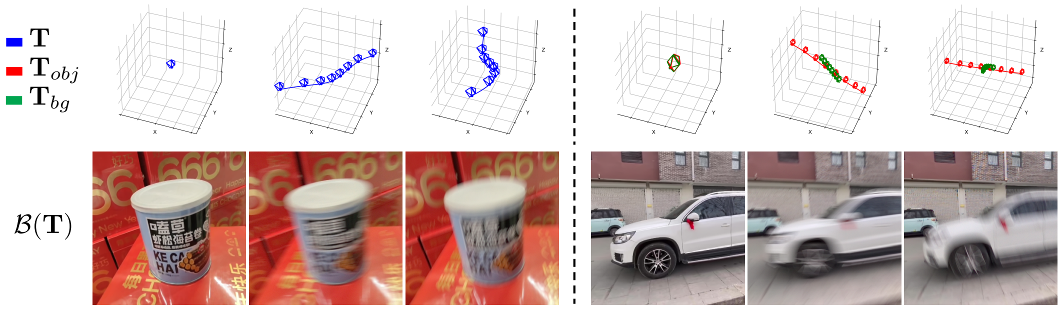

Figure 4: **Visualization of randomly generated 3D trajectories and their corresponding motion-blurred images $\mathcal{B}(\mathbf{T})$. (Left)** By using different trajectories $\mathbf{T}$ for different images, we can generate multiple blurry images corresponding to a single sharp image. Here, we use the same trajectory $\mathbf{T}$ for both the object and the background. **(Right)** By using different motion trajectories for the object and background, $\mathbf{T}_{obj}$ and $\mathbf{T}_{bg}$, respectively, we can simulate rigid-body motion blur. Note that the first and fourth columns in the figure show sharp images with fixed camera views.

camera poses $\{\mathbf{P}_i\}_{i\in\mathcal{N}}$. Here, each scene is trained with the 3DGS model for 30,000 iterations. Then, from the reconstructed 3D scenes, we render an image $\mathcal{I}(\mathbf{P})$ from any arbitrary camera view $\mathbf{P}$. Specifically, to simulate the process of capturing blurry images in real-world scenarios, where moving cameras create blurred images while the shutter is open, we mimic this by moving the camera along a 3D trajectory. We then create the blurry image by accumulating multiple rendered images, each captured by a camera along the motion trajectory. Let $\mathbf{T} = \{\mathbf{P}_\tau\}_{\tau\in[\tau_o,\tau_c]}$ denote continuous camera poses along the trajectory that generates a motion-blurred image $\mathcal{B}(\mathbf{T})$, and we can synthesize the blurred image from rendered sharp images of 3DGS as follow:

$$\mathcal{B}(\mathbf{T}) = g\left(\int_{\tau_o}^{\tau_c} g^{-1}(\mathcal{I}(\mathbf{P}_\tau))d\tau\right) \simeq g\left(\frac{1}{\mathcal{M}}\sum_{t=1}^{\mathcal{M}} g^{-1}(\mathcal{I}(\mathbf{P}_t))\right). \tag{3}$$

Here, the Camera Response Function (CRF) g maps an image from linear RGB space to sRGB space, with g^{-1} being its inverse function. We accumulate rendered sharp images in the linear space and then convert the accumulated blurry image to sRGB space, following the approach in [23, 22]. In real cameras, the RGB color is continuously accumulated while the shutter is open. To simulate this continuous accumulation, we approximate it using a finite sum of $\mathcal{M}$ intermediate sub-frames, which is valid when $\mathcal{M}$ is sufficiently large. Different from the real camera systems, sub-frame rendering through 3DGS does not degrade image quality, regardless of the $\mathcal{M}$ value. In practice, we set $\mathcal{M} = 121$ and select the middle sub-frame as the ground truth sharp image pair. In other words, the sharp images are rendered from a fixed camera position at $\mathbf{P}_{0.5(\tau_o+\tau_c)}$; therefore, a sharp image is represented as $\mathcal{I}(\mathbf{P}_{0.5(\tau_o+\tau_c)})$.

Random Blur Generation. Generating deblur data through novel view synthesis offers the distinct advantage that blurry images can be synthesized from randomly generated camera motions. While any kind of polynomial curve or spline model can function as a camera motion trajectory, we adopt the random-order Bézier curve, which is widely used in prior works [34, 13, 12].

For the camera motion generation given initial camera pose $\mathbf{P}_i$ in training views, we follow the subsequent procedures: 1) Randomly generate a linear motion trajectory in 6 degrees of freedom (6DOF) pose space. 2) Generate an n^{th}-order Bézier curve by randomly perturbing the points that divide the linear motion trajectory into $n + 1$ equal segments. 3) Align the center pose of Bézier curve to be $\mathbf{P}_i$ and sample $\mathcal{M}$ camera poses from the curve. Note that we randomly select the curve parameters $\{n, \delta_t, \delta_r\}$, where $n \in [1, 5]$ denotes the order of Bézier curve, $\delta_t \in \mathbb{R}^3$ represents the length of the curve and $\delta_r \in \mathbb{R}^3$ indicates the shift in orientation, respectively. Here, the 3 dimensions of δ_t and δ_r correspond to the x-, y-, and z-axis of the 3D space.

Since the randomly selected curves, which correspond to camera movements, directly affect the formation of blur, we choose the parameters δ_t and δ_r within pre-defined boundaries to reflect realistic blur. Specifically, we randomly sample the 3D length δ_t from the range $[0, 0.7]$, considering the blur length in previous datasets, and the 3D orientation δ_r from the range [-1.5°, 1.5°], accounting for the minimal impact of rotation during short exposure times in real-world blurry image capturing.

1-to-n blur generation. An additional advantage of the proposed dataset generation is the capability for 1-to-n blur generation. Existing datasets [23, 22, 47, 29] collected with high-speed or beam-splitter cameras typically yield only one blurred image per sharp image or adjust the blur magnitude by altering the number of frames synthesized. In contrast, our method allows for the synthesis of multiple corresponding blurry images for a single sharp image by generating independent trajectories multiple times, which is crucial in preventing overfitting in deblurring architectures. Figure 4 (left) displays examples of multiple (n) blurry images $\mathcal{B}(\mathbf{T})$ corresponding to a single sharp image, using different blur trajectories.

Rigid-body Object Motion Blur. The primary limitation of generating deblur data with 3DGS is its restriction to rendering static scenes, allowing only for motion blur caused by camera movement. However, in real-world blurry images, motion blur often arises from moving objects like pedestrians or vehicles, independent of camera motion. To address this, we leverage the object's binary segmentation mask $\mathbf{m}_s \in \{0, 1\}$ to simulate rigid-body motion. Specifically, we generate two random motion trajectories: one trajectory $\mathbf{T}_{obj}$ to create rigid-body motion blur for the object $\mathcal{B}(\mathbf{T}_{obj})$, and another trajectory $\mathbf{T}_{bg}$ to simulate camera motion blur in the background $\mathcal{B}(\mathbf{T}_{bg})$. Using these two trajectories and the object mask $\mathbf{m}_s$, we apply alpha matting to produce a blurry image where the object and background are distinctly blurred by their respective motions. Here, the alpha value $\mathbf{m}_s(\mathbf{T}_{obj})$ for the mapping is calculated by averaging after 3D warping $\mathbf{m}_s$ along $\mathbf{T}_{obj}$ as follows:

$$\mathbf{m}_s(\mathbf{T}_{obj}) = \sqrt{\frac{1}{\mathcal{M}} \sum_{t=1}^{\mathcal{M}} \pi(\mathbf{m}_s; \mathbf{P}_t)}, \tag{4}$$

$$\mathcal{B}(\mathbf{T}_{obj}, \mathbf{T}_{bg}) = \mathbf{m}_s(\mathbf{T}_{obj}) \cdot \mathcal{B}(\mathbf{T}_{obj}) + (1 - \mathbf{m}_s(\mathbf{T}_{obj})) \cdot \mathcal{B}(\mathbf{T}_{bg}). \tag{5}$$

The object mask of each sub-frame is computed by backward warping [7] $\pi(\mathbf{m}_s; \mathbf{P}_t)$, where the camera intrinsic and the depth and the pose of the sub-frame t are parameters of the warping function $\pi :\in \mathbb{R}^{H\times W} \mapsto \mathbb{R}^{H\times W}$. Note that applying the square-root to the alpha value results in more natural blending at object boundaries, since the background color has already been mixed at the boundaries when synthesizing $\mathcal{B}(\mathbf{T}_{obj})$. Figure 4 (right) shows examples of blurry images $\mathcal{B}(\mathbf{T}_{obj}, \mathbf{T}_{bg})$ generated using different random motion trajectories, $\mathbf{T}_{obj}$ and $\mathbf{T}_{bg}$, for object and background, respectively.

Noise addition. 3DGS employs spherical harmonics to model view-dependent RGB colors, which leads to smooth renderings even when the input images contain slight noise. However, using these smooth renderings to train deblurring deep networks diminishes their generalizability to real-world blurry images, since the networks may fail to learn the necessary features that are typical in naturally occurring noise and complex blur variations. Therefore, we integrate the realistic blur synthesis pipeline introduced in RSBlur [29] to synthesize realistic image noise into the blurred renderings generated from 3DGS. To this end, we convert images from the sRGB space to the camera RAW space, then add Poisson and Gaussian noises, and finally convert them back to the sRGB space, approximating the noise generation principles that occur in real camera systems.

Multi-Resolution. As MVImgNet [43], the source of our GS-Blur, predominantly contains object-centric scenes where objects are often captured close to the camera view, considerable pixels of the rendered images may consist solely of objects. However, during training deblurring network, image patches are typically cropped to smaller size (*e.g.*, 256×256), potentially leading to ineffective training due to the overwhelming presence of objects. To address this, we introduce random down-scaled renderings $\{\times1/2, \times1/3, \times1/4\}$ from the rendered high-resolution images (*e.g.*, 1920×1080) as data augmentation, enabling a broader 3D region to be included within the cropped image patch. However, note that our downsampling differs from that of previous datasets [14, 22], where downsampling is aimed at reducing noise. In our case, we add noise after downsampling.

Finally, we reconstruct $3,408$ scenes from the subset of MVImgNet and train 3DGS to obtain $156,209$ sharp renderings for blur generation. By rendering multiple random blurry pairs and utilizing down-scaled rendering augmentation, we have constructed a GS-Blur dataset consisting of a total of $752,335$ blurry images.

Table 2: **Quantitative comparison of cross-validation regarding PSNR and SSIM.** We train various networks [4, 40, 3] on different training sets and assess their performance in various testing sets. The highest-performing models are indicated in blue, while the second-best performers are highlighted in red. The GS-Blur-trained model demonstrates the best performance across most scenarios, except when the training and testing set exactly match.

	Test Set	GoPro			REDS			BSD			RSBlur		
Train Set	Metrics	MIMO	UFormer	NAFNet	MIMO	UFormer	NAFNet	MIMO	UFormer	NAFNet	MIMO	UFormer	NAFNet
GoPro	PSNR	31.21	32.32	32.81	27.12	29.03	27.26	22.44	27.78	26.25	21.75	27.53	24.97
	SSIM	0.915	0.934	0.960	0.817	0.868	0.872	0.708	0.861	0.831	0.539	0.720	0.727
REDS	PSNR	26.75	27.11	27.67	32.99	32.74	33.49	27.35	26.55	28.08	28.72	27.31	24.93
	SSIM	0.822	0.848	0.903	0.921	0.931	0.946	0.833	0.837	0.873	0.717	0.716	0.739
BSD	PSNR	27.13	28.17	28.38	27.90	28.23	28.23	33.43	33.30	33.87	29.89	30.49	30.63
	SSIM	0.831	0.859	0.909	0.838	0.854	0.886	0.940	0.942	0.953	0.781	0.799	0.843
RSBlur	PSNR	28.50	28.62	30.24	27.67	27.79	28.60	29.72	30.58	31.43	32.52	32.97	33.72
	SSIM	0.868	0.895	0.937	0.830	0.851	0.891	0.897	0.918	0.931	0.836	0.851	0.891
GS-Blur	PSNR	29.44	30.80	31.49	29.55	30.19	30.54	30.42	31.05	31.37	31.17	31.86	32.30
	SSIM	0.882	0.914	0.949	0.876	0.894	0.924	0.910	0.924	0.941	0.812	0.836	0.868

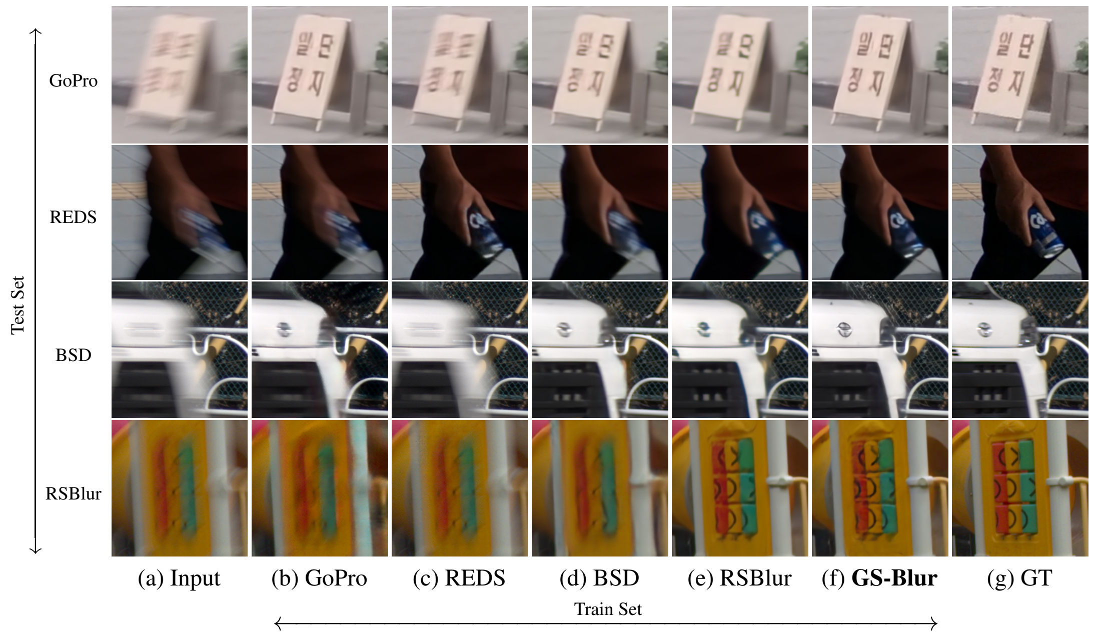

Figure 5: **Qualitative comparison of cross-validation.** We present visual comparisons using NAFNet [3] trained on different datasets, as indicated in the caption. Except when the training and test sets match, the model trained on our GS-Blur (f) consistently produces the most visually appealing results.

4 Experiments

4.1 Implementation details

To evaluate the efficacy of our GS-Blur dataset, we employ recent state-of-the-art deblurring architectures, including Transformer-based architectures (Uformer [40]) and a CNN-based architecture (MIMO-UNet [4] and NAFNet [3]), following their respective training protocols. Specifically, the deblurring networks are trained on random crops of size 256×256, utilizing a batch size of 4 for MIMO-UNet and Uformer and 8 for NAFNet per GPU, with 4 NVIDIA Quadro RTX 8000. Random horizontal and image rotations are also applied to training samples according to each network's protocol, totaling 200k iterations. For Uformer, cosine annealing [19] is employed, starting from $2e^{-4}$ and decaying to $1e^{-6}$, while for NAFNet, it starts from $1e^{-3}$ and decays to $1e^{-6}$. In the case of MIMO-UNet, the learning rate is halved every 30k iterations. For the metrics, we evaluate the results using conventional image quality assessment metrics such as PSNR and SSIM [41].

Table 3: **Quantitative comparison on real blurry images [35].**

Train Set	MUSIQ [16]	TOPIQ [2]
GoPro	37.305	0.262
REDS	38.059	0.261
BSD	45.192	0.318
RSBlur	41.058	0.314
GS-Blur	**48.004**	**0.332**

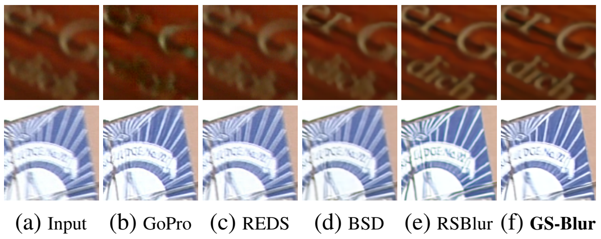

Figure 6: **Visual comparison on real blurry images [35].** Captions represent the training dataset.

Table 4: **Quantitative comparison when training NAFNet [3] on various thresholding strategy.** In the table, 'Failed' refers to 3D scenes with significant drops in PSNR that did not meet the threshold, while 'Passed' refers to scenes with favorable PSNR that successfully passed the threshold.

		GoPro		REDS		BSD		RSBlur	
PSNR thresholding	# Scenes	PSNR	SSIM	PSNR	SSIM	PSNR	SSIM	PSNR	SSIM
Failed	1622	31.01	0.945	30.26	0.919	31.36	0.934	32.05	0.865
Passed + Failed	5030	31.46	0.948	30.52	0.923	**31.42**	0.935	32.13	0.866
Passed (Ours)	3408	**31.49**	**0.949**	**30.54**	**0.924**	31.37	**0.941**	**32.30**	**0.868**

4.2 Reliability of sharp frames

Unlike previous datasets [23, 22, 30, 47, 29], where only blurry images are generated through a synthetic pipeline, both sharp and blurry images in our GS-Blur dataset are synthesized through rendering. As a result, the generated sharp images may contain floating point artifacts that do not accurately represent clean images. To address this, we have measured the PSNR between the ground truth and rendered sharp images for each 3D-reconstructed scene, removing scenes that fall below a certain PSNR threshold. Specifically, if any view showed a PSNR drop of more than 3dB from the mean, the entire scene was classified as failed and excluded from the dataset. This method ensures that only high-quality scenes are included, reducing the impact of floating point-induced blurring in the GS-Blur dataset. Finally, we evaluated our dataset by measuring PSNR and SSIM from multi-view images captured by camera angles not used in 3DGS training, resulting in PSNR=36.73 and SSIM=0.957, confirming the reliability of our sharp frames.

4.3 Generalization of blurry frames

Cross-validation with previous deblurring datasets. To demonstrate that our dataset generalizes well to diverse blurry images, Table 2 compares cross-validation results using our GS-Blur dataset with conventional deblurring datasets, including synthetic [23, 22] and real [47, 29] blurry images. The results indicate that, except when the training and evaluation sets match, models trained on our GS-Blur dataset consistently achieve the best results. This highlights our dataset's generalizability to both synthetically generated and real blurry images, regardless of the used model architectures. Furthermore, Figure 5 shows visual results from various benchmark datasets [23, 22, 47, 29] using NAFNet [3] trained on different datasets. As shown, except when the training and testing sets match, the model trained on our GS-Blur consistently delivers satisfactory results across all benchmark datasets. Please refer to the appendix for visual comparisons using other models [4, 40].

Generalization on real blurry images. While BSD and RSBlur provide realistic blurry images using a beam splitter, their specialized cameras (*e.g.*, machine vision) may differ from other camera models. Therefore, we present a quantitative comparison on real-blurry images [35] in Table 3. Since this dataset contains only blurry images without sharp counterparts, we use recent non-reference-based metrics (*e.g.*, MUSIQ [16] and TOPIQ [2]) for evaluation. As shown, the model trained on our GS-Blur achieves the best results, with visual comparisons available in Figure 6.

Table 5: **Deblurring performance comparison when training NAFNet [3] on GS-Blur with various blur generation pipelines.** The cross marker ✓and ✗indicate whether the corresponding component is applied or not for reconstructing the GS-Blur dataset, respectively. The last row represents our final GS-Blur dataset.

1-to-n blur	Rigid-body obj motion	Noise addition	Multi Resolution	Metrics	GoPro	REDS	BSD	RSBlur
✗	✗	✗	✗	PSNR SSIM	30.69 0.940	30.40 0.921	29.69 0.913	30.18 0.808
✗	✓	✓	✓	PSNR SSIM	31.39 0.948	30.19 0.922	31.13 0.931	32.23 0.867
✓	✗	✓	✓	PSNR SSIM	31.44 0.948	30.27 0.922	31.11 0.931	32.29 0.867
✓	✓	✗	✓	PSNR SSIM	30.97 0.944	**30.94** **0.931**	30.36 0.918	30.99 0.816
✓	✓	✓	✗	PSNR SSIM	31.24 0.947	30.07 0.918	31.06 0.930	32.23 0.867
✓	✓	✓	✓	PSNR SSIM	**31.49** **0.949**	30.54 0.924	**31.37** **0.941**	**32.30** **0.868**

4.4 Ablation studies

We reconstruct blurry images in GS-Blur by excluding 3D scenes under certain PSNR thresholds, 1-to-n blur generation, rigid-body object motion blur, noise addition, and multiple resolutions. This section validates the effectiveness of each component by evaluating the deblurring network [3] trained on our GS-Blur with various modifications on previous benchmark datasets [23, 22, 47, 29]. The overall results are presented in Tables 4 and 5. Specifically, when comparing the last row of Table 4 with the other rows, our PSNR thresholding strategy clearly improves deblurring performance, demonstrating the effectiveness of the components used to reconstruct GS-Blur. Similarly, when comparing the first and last rows of Table 5, our strategy of using four components significantly improves deblurring performance, showing the efficacy of the used components to reconstruct GS-Blur. In the following sections, we illustrate the effectiveness of each component by individually removing them from our final GS-Blur.

PSNR thresholding. As described in Section 4.2, we construct our GS-Blur dataset by excluding 3D scenes with significant drops in PSNR. To demonstrate the effectiveness of this PSNR thresholding strategy, Table 4 compares results for GS-Blur with and without employing PSNR thresholding. When the deblurring network [3] is trained solely on the dataset from failed scenes (the first row of Table 4), there is a clear decline in deblurring performance, indicating that scenes with inaccurate 3D reconstruction (*e.g.*, floating point artifacts) hinder training. In contrast, training on our filtered dataset (the third row of Table 4), which excludes scenes that fall below the PSNR threshold, consistently outperforms the unfiltered dataset (the second row of Table 4), even with fewer scenes. This confirms the effectiveness of our filtering approach.

1-to-n blur generation. Unlike previous datasets [23, 22, 47, 29], which provide only single blurry image per sharp image and may lead to overfitting, GS-Blur can generate multiple (n) blurry images from a single sharp image by varying the motion trajectories (see Figure 4 (left)). As shown in the second row of Table 5, the performance drops consistently without 1-to-n blur generation, as our final approach better aligns with real-world scenarios where diverse blurs can originate from a single sharp image.

Rigid-body object motion. In real-world images, blur is caused not only by camera shake but also by moving objects, resulting in varying motion trajectories across different image pixels. To replicate this scenario, we incorporate rigid-body object motion into the GS-Blur dataset by applying distinct motion trajectories $\mathbf{T}_{obj}$ for objects and $\mathbf{T}_{bg}$ for the background, effectively simulating situations like a moving car captured from a stationary camera (see Figure 4 (right)). Compared to the third row of Table 5, our approach in the last row, which incorporates rigid-body object motion, consistently enhances performance across various benchmark datasets.

Noise addition. Real-world images often contain noise, and adding noise to blurry images can make them more representative of real-world scenarios, leading to improved performance. Specifically, as both synthetic datasets (GoPro [23]) and real datasets (BSD [47] and RSBlur [29]) include noise in their testing sets, training the deblurring network on our noise-added GS-Blur dataset results in mostly better performance, as compared in the fourth and the last rows of Table 5. However, REDS [22] suppresses noise in its evaluation set by downscaling the images by $\frac{2}{3}$, leading to worse performance when the network is trained on the noise-added GS-Blur. Nevertheless, since blurry images from real datasets [47, 29] often contain noise, the addition of noise significantly enhances performance on those datasets.

Multi-resolution. When comparing the fifth and last rows of Table 5, which represent the performance with fixed- and multiple-resolution images in the GS-Blur dataset reconstruction, there is consistent improvement in overall performance with multiple-resolution images. This improvement can be attributed to the characteristics of the MVImgNet dataset [43], which mainly contains objects close to the camera. By incorporating multiple resolutions, our approach effectively simulates various distances between the camera and objects, resulting in more realistic images and consistently better performance across the evaluated metrics.

5 Limitations

While our GS-Blur dataset effectively mimics real blur and demonstrates its value through cross-validation across various benchmark datasets [23, 22, 47, 29], it has two potential limitations. First, although the GS-Blur dataset mimics real blur by moving the camera view along random blur trajectories and simulates rigid-body object motion with different blur trajectories for objects $\mathbf{T}_{obj}$ and background $\mathbf{T}_{bg}$, it cannot consider objects that change shape over time. For example, since the 3D scenes are based on static images, dynamic actions such as the movement of pedestrians' arms and legs during walking or the rotating wheels of a moving vehicle are not represented in GS-Blur. However, by utilizing recent advancements in 4D Gaussian Splatting [42, 8, 17], which can reconstruct temporal 3D scenes from multi-view video inputs, we plan to expand our dataset in future work to include such dynamic changes. Second, unlike conventional sharp images captured directly from cameras, our sharp images are rendered from 3D scenes, which may introduce a gap between them and real-world clean images. Nonetheless, we believe that recent advancements in 3D reconstruction and single-image generation [44, 10] could improve our method, leading to a more accurate dataset reconstruction of our GS-Blur dataset.

6 Conclusion

In this paper, we introduce the GS-Blur dataset, the first deblurring dataset reconstructed from 3D scenes. Unlike previous methods that struggle to obtain diverse blur trajectories, our approach easily simulates various blur trajectories by moving the camera view within the 3D scenes. By using our dataset, we demonstrate improved deblurring quality both qualitatively and quantitatively across various benchmark datasets and deblurring networks, demonstrating the high generalizability of GS-Blur. Furthermore, through extensive experiments, we validate the effectiveness of each component in the pipeline used to reconstruct blurry images in our GS-Blur dataset.

Acknowledgments

This work was supported in part by the IITP grants [No.2021-0-01343, Artificial Intelligence Graduate School Program (Seoul National University), No. 2021-0-02068, and No.2023-0-00156], the NRF grant [No. 2021M3A9E4080782] funded by the Korea government (MSIT), and the SNU-LG AI Research Center.

References

[1] Anpei Chen, Zexiang Xu, Andreas Geiger, Jingyi Yu, and Hao Su. Tensorf: Tensorial radiance fields. In *ECCV*, 2022.

[2] Chaofeng Chen, Jiadi Mo, Jingwen Hou, Haoning Wu, Liang Liao, Wenxiu Sun, Qiong Yan, and Weisi Lin. Topiq: A top-down approach from semantics to distortions for image quality assessment. *arXiv preprint arXiv:2308.03060*, 2023.

[3] Liangyu Chen, Xiaojie Chu, Xiangyu Zhang, and Jian Sun. Simple baselines for image restoration. In *ECCV*, 2022.

[4] Sung-Jin Cho, Seo-Won Ji, Jun-Pyo Hong, Seung-Won Jung, and Sung-Jea Ko. Rethinking coarse-to-fine approach in single image deblurring. In *ICCV*, 2021.

[5] Alexey Dosovitskiy, Lucas Beyer, Alexander Kolesnikov, Dirk Weissenborn, Xiaohua Zhai, Thomas Unterthiner, Mostafa Dehghani, Matthias Minderer, Georg Heigold, Sylvain Gelly, et al. An image is worth 16x16 words: Transformers for image recognition at scale. *arXiv preprint arXiv:2010.11929*, 2020.

[6] Sara Fridovich-Keil, Alex Yu, Matthew Tancik, Qinhong Chen, Benjamin Recht, and Angjoo Kanazawa. Plenoxels: Radiance fields without neural networks. In *CVPR*, 2022.

[7] Richard Hartley and Andrew Zisserman. *Multiple view geometry in computer vision*. Cambridge university press, 2003.

[8] Yi-Hua Huang, Yang-Tian Sun, Ziyi Yang, Xiaoyang Lyu, Yan-Pei Cao, and Xiaojuan Qi. Sc-gs: Sparse-controlled gaussian splatting for editable dynamic scenes. *arXiv preprint arXiv:2312.14937*, 2023.

[9] Bernhard Kerbl, Georgios Kopanas, Thomas Leimkühler, and George Drettakis. 3d gaussian splatting for real-time radiance field rendering. *ACM TOG*, 42(4), 2023.

[10] Shakiba Kheradmand, Daniel Rebain, Gopal Sharma, Weiwei Sun, Jeff Tseng, Hossam Isack, Abhishek Kar, Andrea Tagliasacchi, and Kwang Moo Yi. 3d gaussian splatting as markov chain monte carlo. *arXiv preprint arXiv:2404.09591*, 2024.

[11] Orest Kupyn, Volodymyr Budzan, Mykola Mykhailych, Dmytro Mishkin, and Jiří Matas. Deblurgan: Blind motion deblurring using conditional adversarial networks. In *CVPR*, 2018.

[12] Dongwoo Lee, Jeongtaek Oh, Jaesung Rim, Sunghyun Cho, and Kyoung Mu Lee. Exblurf: Efficient radiance fields for extreme motion blurred images. In *ICCV*, 2023.

[13] Dongwoo Lee, Haesol Park, In Kyu Park, and Kyoung Mu Lee. Joint blind motion deblurring and depth estimation of light field. In *ECCV*, 2018.

[14] Dongxu Li, Chenchen Xu, Kaihao Zhang, Xin Yu, Yiran Zhong, Wenqi Ren, Hanna Suominen, and Hongdong Li. Arvo: Learning all-range volumetric correspondence for video deblurring. In *CVPR*, 2021.

[15] Jingyun Liang, Jiezhang Cao, Guolei Sun, Kai Zhang, Luc Van Gool, and Radu Timofte. Swinir: Image restoration using swin transformer. In *ICCV*, 2021.

[16] Jingyun Liang, Kai Zhang, Shuhang Gu, Luc Van Gool, and Radu Timofte. Flow-based kernel prior with application to blind super-resolution. In *CVPR*, 2021.

[17] Youtian Lin, Zuozhuo Dai, Siyu Zhu, and Yao Yao. Gaussian-flow: 4d reconstruction with dynamic 3d gaussian particle. *arXiv preprint arXiv:2312.03431*, 2023.

[18] Ze Liu, Yutong Lin, Yue Cao, Han Hu, Yixuan Wei, Zheng Zhang, Stephen Lin, and Baining Guo. Swin transformer: Hierarchical vision transformer using shifted windows. In *ICCV*, 2021.

[19] Ilya Loshchilov and Frank Hutter. Sgdr: Stochastic gradient descent with warm restarts. *arXiv preprint arXiv:1608.03983*, 2016.

[20] Ben Mildenhall, Pratul P Srinivasan, Matthew Tancik, Jonathan T Barron, Ravi Ramamoorthi, and Ren Ng. Nerf: Representing scenes as neural radiance fields for view synthesis. In *ECCV*, 2020.

[21] Thomas Müller, Alex Evans, Christoph Schied, and Alexander Keller. Instant neural graphics primitives with a multiresolution hash encoding. *ACM transactions on graphics (TOG)*, 41(4):1–15, 2022.

[22] Seungjun Nah, Sungyong Baik, Seokil Hong, Gyeongsik Moon, Sanghyun Son, Radu Timofte, and Kyoung Mu Lee. Ntire 2019 challenge on video deblurring and super-resolution: Dataset and study. In *CVPR Workshops*, 2019.

[23] Seungjun Nah, Tae Hyun Kim, and Kyoung Mu Lee. Deep multi-scale convolutional neural network for dynamic scene deblurring. In *CVPR*, 2017.

[24] Jeongtaek Oh, Jaeyoung Chung, Dongwoo Lee, and Kyoung Mu Lee. Deblurgs: Gaussian splatting for camera motion blur. *arXiv preprint arXiv:2404.11358*, 2024.

[25] Joonkyu Park, Gyeongsik Moon, Weipeng Xu, Evan Kaseman, Takaaki Shiratori, and Kyoung Mu Lee. 3d hand sequence recovery from real blurry images and event stream. *ECCV*, 2024.

[26] JoonKyu Park, Seungjun Nah, and Kyoung Mu Lee. Pay attention to hidden states for video deblurring: Ping-pong recurrent neural networks and selective non-local attention. *arXiv preprint arXiv:2203.16063*, 2022.

[27] Joonkyu Park, Seungjun Nah, and Kyoung Mu Lee. Recurrence-in-recurrence networks for video deblurring. *BMVC*, 2022.

[28] Cheng Peng, Yutao Tang, Yifan Zhou, Nengyu Wang, Xijun Liu, Deming Li, and Rama Chellappa. Bags: Blur agnostic gaussian splatting through multi-scale kernel modeling. *ECCV*, 2024.

[29] Jaesung Rim, Geonung Kim, Jungeon Kim, Junyong Lee, Seungyong Lee, and Sunghyun Cho. Realistic blur synthesis for learning image deblurring. In *ECCV*. Springer, 2022.

[30] Jaesung Rim, Haeyun Lee, Jucheol Won, and Sunghyun Cho. Real-world blur dataset for learning and benchmarking deblurring algorithms. In *ECCV*, 2020.

[31] Denys Rozumnyi, Martin R Oswald, Vittorio Ferrari, and Marc Pollefeys. Motion-from-blur: 3d shape and motion estimation of motion-blurred objects in videos. In *CVPR*, 2022.

[32] Johannes L Schonberger and Jan-Michael Frahm. Structure-from-motion revisited. In *CVPR*, 2016.

[33] Ziyi Shen, Wenguan Wang, Xiankai Lu, Jianbing Shen, Haibin Ling, Tingfa Xu, and Ling Shao. Human-aware motion deblurring. In *ICCV*, 2019.

[34] Pratul P Srinivasan, Ren Ng, and Ravi Ramamoorthi. Light field blind motion deblurring. In *CVPR*, 2017.

[35] Shuochen Su, Mauricio Delbracio, Jue Wang, Guillermo Sapiro, Wolfgang Heidrich, and Oliver Wang. Deep video deblurring for hand-held cameras. In *CVPR*, 2017.

[36] Cheng Sun, Min Sun, and Hwann-Tzong Chen. Direct voxel grid optimization: Super-fast convergence for radiance fields reconstruction. In *CVPR*, 2022.

[37] Xin Tao, Hongyun Gao, Xiaoyong Shen, Jue Wang, and Jiaya Jia. Scale-recurrent network for deep image deblurring. In *CVPR*, 2018.

[38] Zachary Teed and Jia Deng. Raft: Recurrent all-pairs field transforms for optical flow. In *ECCV*, 2020.

[39] Laurens Van der Maaten and Geoffrey Hinton. Visualizing data using t-sne. *JMLR*, 9(11), 2008.

[40] Zhendong Wang, Xiaodong Cun, Jianmin Bao, Wengang Zhou, Jianzhuang Liu, and Houqiang Li. Uformer: A general u-shaped transformer for image restoration. In *CVPR*, 2022.

[41] Zhou Wang, Alan C Bovik, Hamid R Sheikh, and Eero P Simoncelli. Image quality assessment: from error visibility to structural similarity. *IEEE transactions on image processing*, 13(4):600–612, 2004.

[42] Guanjun Wu, Taoran Yi, Jiemin Fang, Lingxi Xie, Xiaopeng Zhang, Wei Wei, Wenyu Liu, Qi Tian, and Xinggang Wang. 4d gaussian splatting for real-time dynamic scene rendering. *arXiv preprint arXiv:2310.08528*, 2023.

[43] Xianggang Yu, Mutian Xu, Yidan Zhang, Haolin Liu, Chongjie Ye, Yushuang Wu, Zizheng Yan, Chenming Zhu, Zhangyang Xiong, Tianyou Liang, et al. Mvimgnet: A large-scale dataset of multi-view images. In *CVPR*, 2023.

[44] Zehao Yu, Anpei Chen, Binbin Huang, Torsten Sattler, and Andreas Geiger. Mip-splatting: Alias-free 3d gaussian splatting. In *CVPR*, 2024.

[45] Syed Waqas Zamir, Aditya Arora, Salman Khan, Munawar Hayat, Fahad Shahbaz Khan, and Ming-Hsuan Yang. Restormer: Efficient transformer for high-resolution image restoration. In *CVPR*, 2022.

[46] Kaihao Zhang, Tao Wang, Wenhan Luo, Wenqi Ren, Björn Stenger, Wei Liu, Hongdong Li, and Ming-Hsuan Yang. Mc-blur: a comprehensive benchmark for image deblurring. *TCSVT*, 2023.

[47] Zhihang Zhong, Ye Gao, Yinqiang Zheng, and Bo Zheng. Efficient spatio-temporal recurrent neural network for video deblurring. In *ECCV*, 2020.

[48] Matthias Zwicker, Hanspeter Pfister, Jeroen Van Baar, and Markus Gross. Ewa splatting. *TVCG*, 8(3), 2002.

Appendices

A Additional visual comparison of cross-validation

Figures 7, 8, and 9 present a comprehensive qualitative comparison of cross-validation results using three different deblurring models: MIMO-UNet [4], UFormer [40], and NAFNet [3]. These extensive qualitative results highlight the effectiveness of our proposed GS-Blur dataset in enhancing the generalizability of deblurring for real-world motion blur.

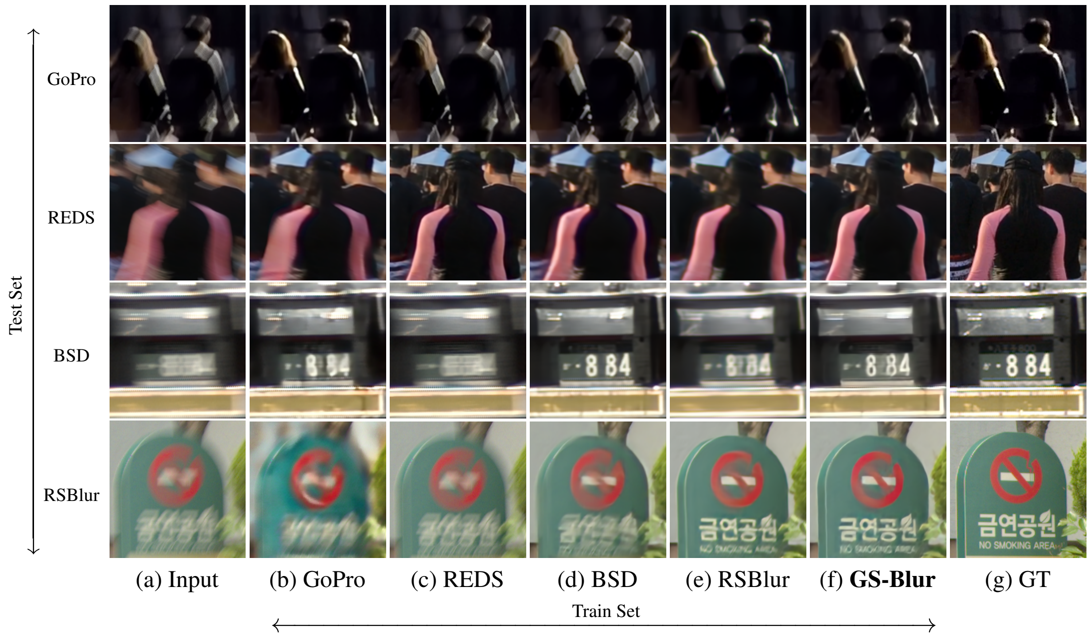

Figure 7: **Qualitative comparison of cross-validation using MIMO-UNet [4].**

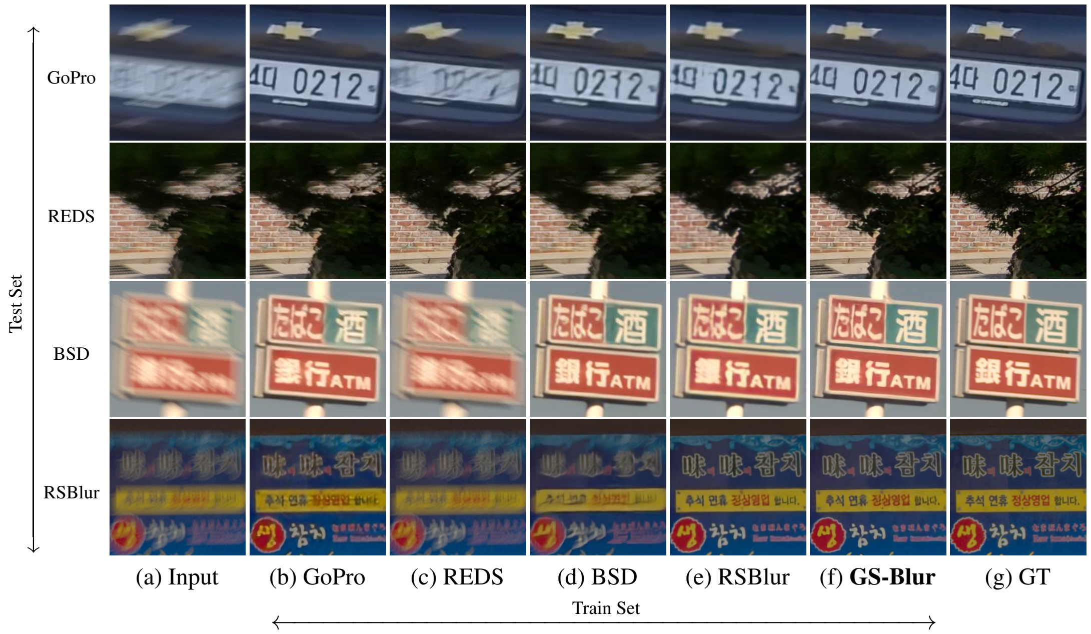

Figure 8: **Qualitative comparison of cross-validation using UFormer [40].**

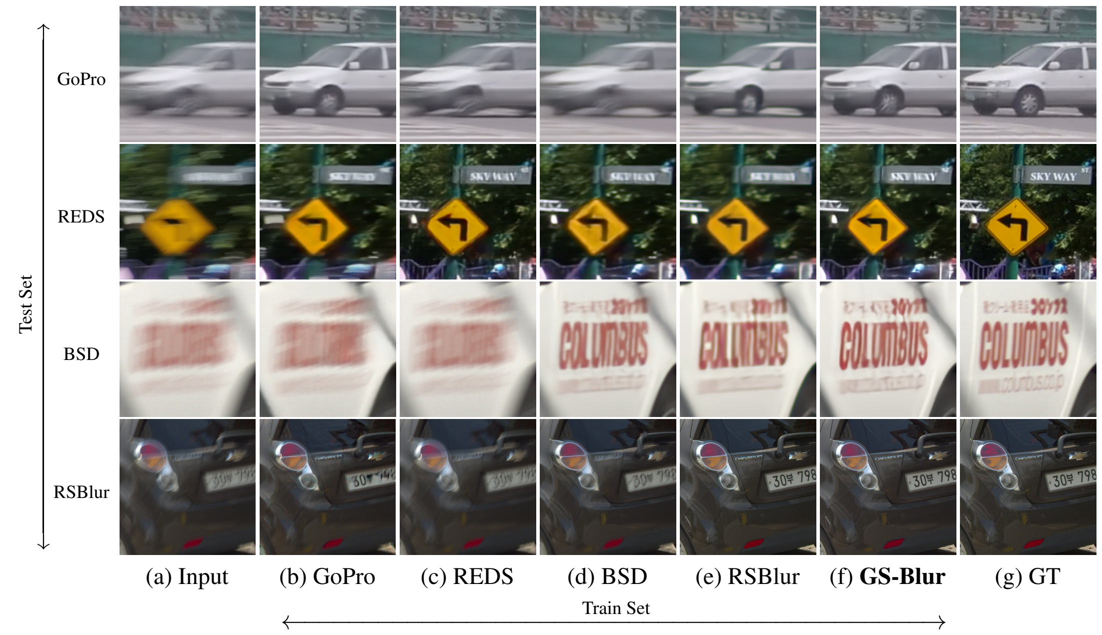

Figure 9: **Qualitative comparison of cross-validation using NAFNet [3].**

B Selected Classes from MVImgNet

We selected 26 classes from MVImgNet [43] that contain rich 3D information and textures when generating GS-Blur dataset. The IDs and names of the selected classes are as follows: {6: table, 8: sofa, 14: flowerpot, 17: mug, 26: pot, 28: guitar, 29: bookshelf, 36: chair, 37: car, 38: cap, 39: can, 41: cabinet, 44: bicycle, 45: bench, 46: bed, 52: plush toy, 93: coat rack, 112: ladder, 137: rockery, 152: strings, 155: scarf, 156: shoe, 158: pants, 159: clothing}

C Additional visualization of GS-Blur

In Figure 10 we provide a comprehensive visualization of all the classes we generated in the GS-Blur dataset. This figure highlights the diversity and richness of the dataset across various scenes and blur patterns.

D Negative societal impact

While advanced deblurring algorithms facilitate easy image enhancement for the general public, their use also raises concerns about potentially malicious applications, particularly regarding privacy issues. Blurring is commonly employed to protect personal information, such as faces and personal IDs. To address potential misuse, image forensic algorithms can be employed, which aim to authenticate images. Many of these algorithms focus on training classifiers to differentiate between images captured in the real world and those processed by deep learning models.

E License of the used assets

- 3D Gaussian-splatting is a publicly available dataset released under CC BY MIT license.
- MVImgNet dataset is a publicly available dataset released under CC BY 4.0 license.
- GoPro dataset is a publicly available dataset released under CC BY 4.0 license.
- REDS dataset is a publicly available dataset released under CC BY 4.0 license.
- BSD dataset is a publicly available dataset released under CC BY MIT license.
- RSBlur dataset is a publicly available dataset released under CC BY MIT license.

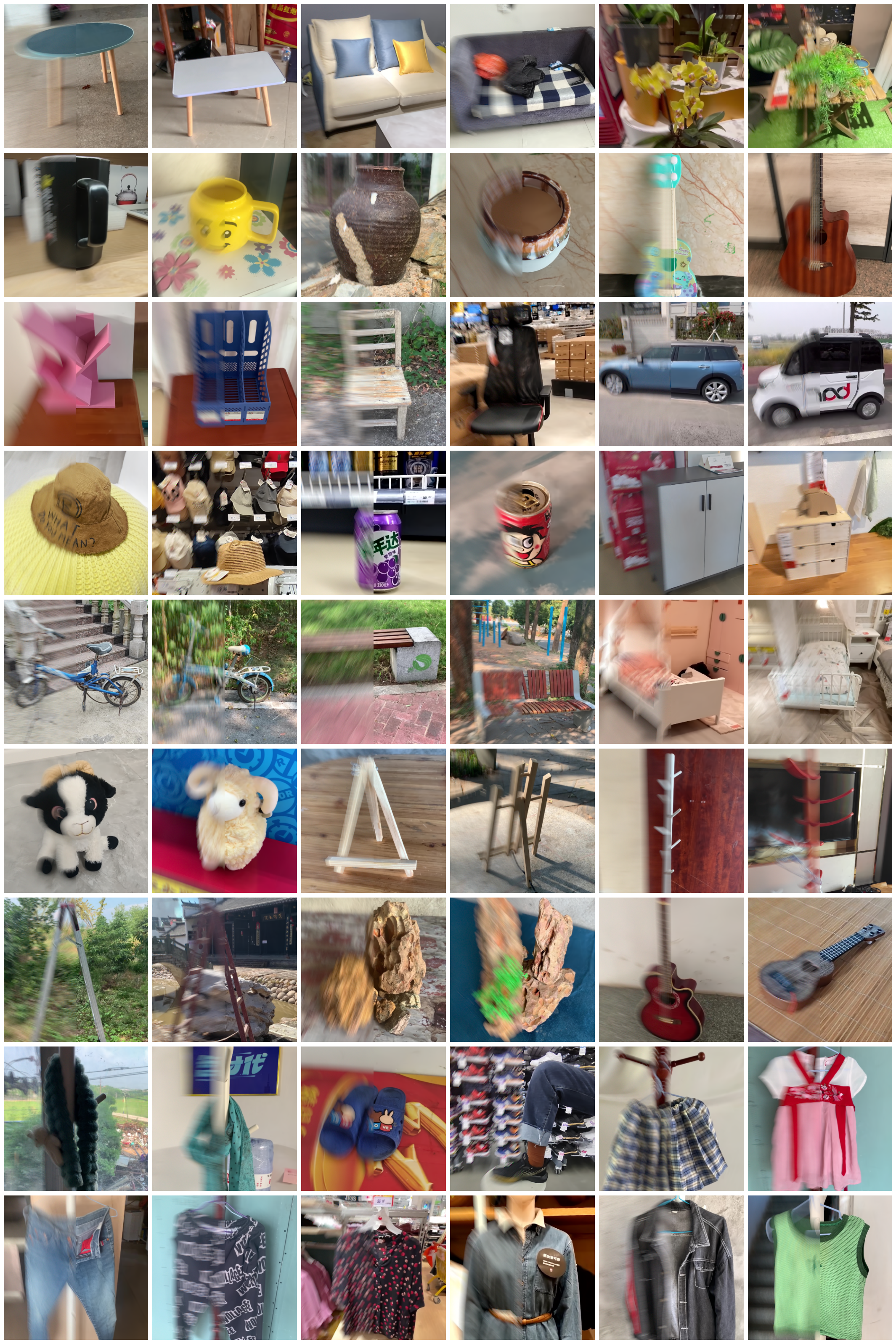

Figure 10: **Examples of the proposed GS-Blur dataset.** The left half of the frames displays synthetically generated blur, while the right half exhibits sharpness.

NeurIPS Paper Checklist

1. **Claims**

   Question: Do the main claims made in the abstract and introduction accurately reflect the paper's contributions and scope?

   Answer: [Yes]

   Justification: We analyzed the limitations of existing deblurring datasets and proposed a novel dataset using 3D rendering techniques to address these limitations. We experimentally demonstrated that the proposed dataset can compensate for the weaknesses of existing datasets in terms of generalizability.

   Guidelines:

   - The answer NA means that the abstract and introduction do not include the claims made in the paper.
   - The abstract and/or introduction should clearly state the claims made, including the contributions made in the paper and important assumptions and limitations. A No or NA answer to this question will not be perceived well by the reviewers.
   - The claims made should match theoretical and experimental results, and reflect how much the results can be expected to generalize to other settings.
   - It is fine to include aspirational goals as motivation as long as it is clear that these goals are not attained by the paper.

2. **Limitations**

   Question: Does the paper discuss the limitations of the work performed by the authors?

   Answer: [Yes] ,

   Justification: See Section 5.

   Guidelines:

   - The answer NA means that the paper has no limitation while the answer No means that the paper has limitations, but those are not discussed in the paper.
   - The authors are encouraged to create a separate "Limitations" section in their paper.
   - The paper should point out any strong assumptions and how robust the results are to violations of these assumptions (e.g., independence assumptions, noiseless settings, model well-specification, asymptotic approximations only holding locally). The authors should reflect on how these assumptions might be violated in practice and what the implications would be.
   - The authors should reflect on the scope of the claims made, e.g., if the approach was only tested on a few datasets or with a few runs. In general, empirical results often depend on implicit assumptions, which should be articulated.
   - The authors should reflect on the factors that influence the performance of the approach. For example, a facial recognition algorithm may perform poorly when image resolution is low or images are taken in low lighting. Or a speech-to-text system might not be used reliably to provide closed captions for online lectures because it fails to handle technical jargon.
   - The authors should discuss the computational efficiency of the proposed algorithms and how they scale with dataset size.
   - If applicable, the authors should discuss possible limitations of their approach to address problems of privacy and fairness.
   - While the authors might fear that complete honesty about limitations might be used by reviewers as grounds for rejection, a worse outcome might be that reviewers discover limitations that aren't acknowledged in the paper. The authors should use their best judgment and recognize that individual actions in favor of transparency play an important role in developing norms that preserve the integrity of the community. Reviewers will be specifically instructed to not penalize honesty concerning limitations.

3. **Theory Assumptions and Proofs**

   Question: For each theoretical result, does the paper provide the full set of assumptions and a complete (and correct) proof?

Answer: [NA]

Justification:

Guidelines:

- The answer NA means that the paper does not include theoretical results.
- All the theorems, formulas, and proofs in the paper should be numbered and cross-referenced.
- All assumptions should be clearly stated or referenced in the statement of any theorems.
- The proofs can either appear in the main paper or the supplemental material, but if they appear in the supplemental material, the authors are encouraged to provide a short proof sketch to provide intuition.
- Inversely, any informal proof provided in the core of the paper should be complemented by formal proofs provided in appendix or supplemental material.
- Theorems and Lemmas that the proof relies upon should be properly referenced.

4. **Experimental Result Reproducibility**

   Question: Does the paper fully disclose all the information needed to reproduce the main experimental results of the paper to the extent that it affects the main claims and/or conclusions of the paper (regardless of whether the code and data are provided or not)?

   Answer: [Yes]

   Justification: In Section 3, we described the 3D volume rendering, blur model, and data augmentation we used, and specify the hyperparameters to reproduce the proposed pipeline. We also specify the configuration for training the deep networks used in our experiments.

   Guidelines:

   - The answer NA means that the paper does not include experiments.
   - If the paper includes experiments, a No answer to this question will not be perceived well by the reviewers: Making the paper reproducible is important, regardless of whether the code and data are provided or not.
   - If the contribution is a dataset and/or model, the authors should describe the steps taken to make their results reproducible or verifiable.
   - Depending on the contribution, reproducibility can be accomplished in various ways. For example, if the contribution is a novel architecture, describing the architecture fully might suffice, or if the contribution is a specific model and empirical evaluation, it may be necessary to either make it possible for others to replicate the model with the same dataset, or provide access to the model. In general. releasing code and data is often one good way to accomplish this, but reproducibility can also be provided via detailed instructions for how to replicate the results, access to a hosted model (e.g., in the case of a large language model), releasing of a model checkpoint, or other means that are appropriate to the research performed.
   - While NeurIPS does not require releasing code, the conference does require all submissions to provide some reasonable avenue for reproducibility, which may depend on the nature of the contribution. For example
     (a) If the contribution is primarily a new algorithm, the paper should make it clear how to reproduce that algorithm.
     (b) If the contribution is primarily a new model architecture, the paper should describe the architecture clearly and fully.
     (c) If the contribution is a new model (e.g., a large language model), then there should either be a way to access this model for reproducing the results or a way to reproduce the model (e.g., with an open-source dataset or instructions for how to construct the dataset).
     (d) We recognize that reproducibility may be tricky in some cases, in which case authors are welcome to describe the particular way they provide for reproducibility. In the case of closed-source models, it may be that access to the model is limited in some way (e.g., to registered users), but it should be possible for other researchers to have some path to reproducing or verifying the results.

5. **Open access to data and code**

Question: Does the paper provide open access to the data and code, with sufficient instructions to faithfully reproduce the main experimental results, as described in supplemental material?

Answer: [No]

Justification: Upon acceptance, we will publicly release our dataset and code to reproduce the data generation.

Guidelines:

- The answer NA means that paper does not include experiments requiring code.
- Please see the NeurIPS code and data submission guidelines (`https://nips.cc/public/guides/CodeSubmissionPolicy`) for more details.
- While we encourage the release of code and data, we understand that this might not be possible, so "No" is an acceptable answer. Papers cannot be rejected simply for not including code, unless this is central to the contribution (e.g., for a new open-source benchmark).
- The instructions should contain the exact command and environment needed to run to reproduce the results. See the NeurIPS code and data submission guidelines (`https://nips.cc/public/guides/CodeSubmissionPolicy`) for more details.
- The authors should provide instructions on data access and preparation, including how to access the raw data, preprocessed data, intermediate data, and generated data, etc.
- The authors should provide scripts to reproduce all experimental results for the new proposed method and baselines. If only a subset of experiments are reproducible, they should state which ones are omitted from the script and why.
- At submission time, to preserve anonymity, the authors should release anonymized versions (if applicable).
- Providing as much information as possible in supplemental material (appended to the paper) is recommended, but including URLs to data and code is permitted.

6. **Experimental Setting/Details**

Question: Does the paper specify all the training and test details (e.g., data splits, hyperparameters, how they were chosen, type of optimizer, etc.) necessary to understand the results?

Answer: [Yes]

Justification: We specified our expermental setting in Section 4.

Guidelines:

- The answer NA means that the paper does not include experiments.
- The experimental setting should be presented in the core of the paper to a level of detail that is necessary to appreciate the results and make sense of them.
- The full details can be provided either with the code, in appendix, or as supplemental material.

7. **Experiment Statistical Significance**

Question: Does the paper report error bars suitably and correctly defined or other appropriate information about the statistical significance of the experiments?

Answer: [No]

Justification:

Guidelines:

- The answer NA means that the paper does not include experiments.
- The authors should answer "Yes" if the results are accompanied by error bars, confidence intervals, or statistical significance tests, at least for the experiments that support the main claims of the paper.
- The factors of variability that the error bars are capturing should be clearly stated (for example, train/test split, initialization, random drawing of some parameter, or overall run with given experimental conditions).

- The method for calculating the error bars should be explained (closed form formula, call to a library function, bootstrap, etc.)
- The assumptions made should be given (e.g., Normally distributed errors).
- It should be clear whether the error bar is the standard deviation or the standard error of the mean.
- It is OK to report 1-sigma error bars, but one should state it. The authors should preferably report a 2-sigma error bar than state that they have a 96% CI, if the hypothesis of Normality of errors is not verified.
- For asymmetric distributions, the authors should be careful not to show in tables or figures symmetric error bars that would yield results that are out of range (e.g. negative error rates).
- If error bars are reported in tables or plots, The authors should explain in the text how they were calculated and reference the corresponding figures or tables in the text.

8. **Experiments Compute Resources**

   Question: For each experiment, does the paper provide sufficient information on the computer resources (type of compute workers, memory, time of execution) needed to reproduce the experiments?

   Answer: [Yes]

   Justification: We specified our experimental setup in Section 4.

   Guidelines:

   - The answer NA means that the paper does not include experiments.
   - The paper should indicate the type of compute workers CPU or GPU, internal cluster, or cloud provider, including relevant memory and storage.
   - The paper should provide the amount of compute required for each of the individual experimental runs as well as estimate the total compute.
   - The paper should disclose whether the full research project required more compute than the experiments reported in the paper (e.g., preliminary or failed experiments that didn't make it into the paper).

9. **Code Of Ethics**

   Question: Does the research conducted in the paper conform, in every respect, with the NeurIPS Code of Ethics https://neurips.cc/public/EthicsGuidelines?

   Answer: [Yes]

   Justification: We carefully read NeurIPS Code of Ethics and followed the guidelines. We preserve anonymity in all respects.

   Guidelines:

   - The answer NA means that the authors have not reviewed the NeurIPS Code of Ethics.
   - If the authors answer No, they should explain the special circumstances that require a deviation from the Code of Ethics.
   - The authors should make sure to preserve anonymity (e.g., if there is a special consideration due to laws or regulations in their jurisdiction).

10. **Broader Impacts**

    Question: Does the paper discuss both potential positive societal impacts and negative societal impacts of the work performed?

    Answer: [Yes]

    Justification: See Section D in the appendix.

    Guidelines:

    - The answer NA means that there is no societal impact of the work performed.
    - If the authors answer NA or No, they should explain why their work has no societal impact or why the paper does not address societal impact.

- Examples of negative societal impacts include potential malicious or unintended uses (e.g., disinformation, generating fake profiles, surveillance), fairness considerations (e.g., deployment of technologies that could make decisions that unfairly impact specific groups), privacy considerations, and security considerations.
- The conference expects that many papers will be foundational research and not tied to particular applications, let alone deployments. However, if there is a direct path to any negative applications, the authors should point it out. For example, it is legitimate to point out that an improvement in the quality of generative models could be used to generate deepfakes for disinformation. On the other hand, it is not needed to point out that a generic algorithm for optimizing neural networks could enable people to train models that generate Deepfakes faster.
- The authors should consider possible harms that could arise when the technology is being used as intended and functioning correctly, harms that could arise when the technology is being used as intended but gives incorrect results, and harms following from (intentional or unintentional) misuse of the technology.
- If there are negative societal impacts, the authors could also discuss possible mitigation strategies (e.g., gated release of models, providing defenses in addition to attacks, mechanisms for monitoring misuse, mechanisms to monitor how a system learns from feedback over time, improving the efficiency and accessibility of ML).

11. **Safeguards**

    Question: Does the paper describe safeguards that have been put in place for responsible release of data or models that have a high risk for misuse (e.g., pretrained language models, image generators, or scraped datasets)?

    Answer: [NA]

    Justification:

    Guidelines:

    - The answer NA means that the paper poses no such risks.
    - Released models that have a high risk for misuse or dual-use should be released with necessary safeguards to allow for controlled use of the model, for example by requiring that users adhere to usage guidelines or restrictions to access the model or implementing safety filters.
    - Datasets that have been scraped from the Internet could pose safety risks. The authors should describe how they avoided releasing unsafe images.
    - We recognize that providing effective safeguards is challenging, and many papers do not require this, but we encourage authors to take this into account and make a best faith effort.

12. **Licenses for existing assets**

    Question: Are the creators or original owners of assets (e.g., code, data, models), used in the paper, properly credited and are the license and terms of use explicitly mentioned and properly respected?

    Answer: [Yes]

    Justification: See Section E in the appendix.

    Guidelines:

    - The answer NA means that the paper does not use existing assets.
    - The authors should cite the original paper that produced the code package or dataset.
    - The authors should state which version of the asset is used and, if possible, include a URL.
    - The name of the license (e.g., CC-BY 4.0) should be included for each asset.
    - For scraped data from a particular source (e.g., website), the copyright and terms of service of that source should be provided.
    - If assets are released, the license, copyright information, and terms of use in the package should be provided. For popular datasets, `paperswithcode.com/datasets` has curated licenses for some datasets. Their licensing guide can help determine the license of a dataset.

- For existing datasets that are re-packaged, both the original license and the license of the derived asset (if it has changed) should be provided.
- If this information is not available online, the authors are encouraged to reach out to the asset's creators.

13. **New Assets**

    Question: Are new assets introduced in the paper well documented and is the documentation provided alongside the assets?

    Answer: [No]

    Justification: Documentation for the proposed dataset and generation method will be uploaded upon acceptance.

    Guidelines:

    - The answer NA means that the paper does not release new assets.
    - Researchers should communicate the details of the dataset/code/model as part of their submissions via structured templates. This includes details about training, license, limitations, etc.
    - The paper should discuss whether and how consent was obtained from people whose asset is used.
    - At submission time, remember to anonymize your assets (if applicable). You can either create an anonymized URL or include an anonymized zip file.

14. **Crowdsourcing and Research with Human Subjects**

    Question: For crowdsourcing experiments and research with human subjects, does the paper include the full text of instructions given to participants and screenshots, if applicable, as well as details about compensation (if any)?

    Answer: [NA]

    Justification:

    Guidelines:

    - The answer NA means that the paper does not involve crowdsourcing nor research with human subjects.
    - Including this information in the supplemental material is fine, but if the main contribution of the paper involves human subjects, then as much detail as possible should be included in the main paper.
    - According to the NeurIPS Code of Ethics, workers involved in data collection, curation, or other labor should be paid at least the minimum wage in the country of the data collector.

15. **Institutional Review Board (IRB) Approvals or Equivalent for Research with Human Subjects**

    Question: Does the paper describe potential risks incurred by study participants, whether such risks were disclosed to the subjects, and whether Institutional Review Board (IRB) approvals (or an equivalent approval/review based on the requirements of your country or institution) were obtained?

    Answer: [NA]

    Justification:

    Guidelines:

    - The answer NA means that the paper does not involve crowdsourcing nor research with human subjects.
    - Depending on the country in which research is conducted, IRB approval (or equivalent) may be required for any human subjects research. If you obtained IRB approval, you should clearly state this in the paper.
    - We recognize that the procedures for this may vary significantly between institutions and locations, and we expect authors to adhere to the NeurIPS Code of Ethics and the guidelines for their institution.
    - For initial submissions, do not include any information that would break anonymity (if applicable), such as the institution conducting the review.